

Vinculin tension distributions of individual stress fibers within cell–matrix adhesions

Ching-Wei Chang and Sanjay Kumar*

Department of Bioengineering, University of California Berkeley, Berkeley, CA 94720, USA

*Author for correspondence (skumar@berkeley.edu)

Accepted 17 April 2013

Journal of Cell Science 126, 3021–3030

© 2013. Published by The Company of Biologists Ltd

doi: 10.1242/jcs.119032

Summary

Actomyosin stress fibers (SFs) enable cells to exert traction on planar extracellular matrices (ECMs) by tensing focal adhesions (FAs) at the cell–ECM interface. Although it is widely appreciated that the spatial and temporal distribution of these tensile forces play key roles in polarity, motility, fate choice, and other defining cell behaviors, virtually nothing is known about how an individual SF quantitatively contributes to tensile loads borne by specific molecules within associated FAs. We address this key open question by using femtosecond laser ablation to sever single SFs in cells while tracking tension across vinculin using a molecular optical sensor. We show that disruption of a single SF reduces tension across vinculin in FAs located throughout the cell, with enriched vinculin tension reduction in FAs oriented parallel to the targeted SF. Remarkably, however, some subpopulations of FAs exhibit enhanced vinculin tension upon SF irradiation and undergo dramatic, unexpected transitions between tension-enhanced and tension-reduced states. These changes depend strongly on the location of the severed SF, consistent with our earlier finding that different SF pools are regulated by distinct myosin activators. We critically discuss the extent to which these measurements can be interpreted in terms of whole-FA tension and traction and propose a model that relates SF tension to adhesive loads and cell shape stability. These studies represent the most direct and high-resolution intracellular measurements of SF contributions to tension on specific FA proteins to date and offer a new paradigm for investigating regulation of adhesive complexes by cytoskeletal force.

Key words: Cell mechanics, Mechanotransduction, Stress fibers, Focal adhesions, Laser ablation, Fluorescence resonance energy transfer

Introduction

Over the past decade, it has become clear that the application of tensile force by cells on their surroundings plays key roles in cell shape determination, motility, and fate decisions (Dupont et al., 2011; Fu et al., 2010; Levental et al., 2009; Prager-Khoutorsky et al., 2011). Mammalian cells cultured on solid supports generate these tensile forces in part through contractile stress fibers (SFs), which are assemblies of filamentous actin (F-actin), actin-binding proteins, and myosin motors. SFs contribute to cytoskeletal pre-stress by anchoring into focal adhesions (FAs) at the cell–extracellular matrix (ECM) interface, which in turn enables the cell to generate traction against its microenvironment (Deguchi et al., 2006; Etienne-Manneville and Hall, 2002; Hotulainen and Lappalainen, 2006). While the molecular mechanisms through which FAs sense and transmit tensile forces between SFs and the ECM remain controversial, it is known that some FA proteins can undergo load-dependent conformational changes, which can trigger biochemical events critical to downstream signaling such as phosphorylation and protein–protein binding (Cohen et al., 2006; Hytönen and Vogel, 2008; Sawada et al., 2006; Vogel, 2006). Thus, understanding cell–ECM mechanotransduction requires insight into how tensile forces generated by single SFs are spatially distributed across these molecular mechanosensors within FAs, where they may ultimately contribute to downstream signaling.

We and others have found femtosecond laser nanosurgery to be a powerful tool for measuring the contractile properties of single SFs in living cells (Colombelli et al., 2009; Colombelli et al.,

2006; Kumar et al., 2006; Lele et al., 2006; Rauzi et al., 2008; Ronchi et al., 2012; Russell et al., 2009; Tanner et al., 2010). In this method, a cellular SF is visualized and irradiated with a femtosecond laser, resulting in SF scission and retraction. The retraction dynamics yield quantitative information about the viscoelastic properties of the fiber, and the resulting change in cell shape lends insight into the contribution of the targeted SF to cell shape stability. We have previously used this approach to demonstrate that the mechanical properties of a SF depend strongly on whether the fiber is located at the cell center or periphery (Tanner et al., 2010), and that this is related to the differential control of these two SF populations by the myosin activators Rho-associated kinase (ROCK) and myosin light chain kinase (MLCK), respectively (Katoh et al., 2011; Katoh et al., 2007; Totsukawa et al., 2004). Moreover, disruption of peripheral SFs often triggers whole-cell adhesive disassembly and contraction, which has led us to speculate that central and peripheral SFs distribute their tensile loads differently across the cell–ECM interface and that this in turn gives rise to their differential contributions to cell shape stability. This could potentially be accompanied by and reflected in changes in tension across specific mechanosensors within individual FAs.

Genetically encoded probes, particularly those based on fluorescence resonance energy transfer (FRET), have now made it possible to directly visualize the activation of specific cellular signal transduction pathways in a spatially and temporally defined fashion. Most notably, Grashoff et al., recently developed a FRET sensor of tension-induced strain

within the FA protein vinculin, which is capable of sensing piconewton (pN) loads in migrating cells (Grashoff et al., 2010). In this vinculin tension sensor (VinTS), the vinculin head and tail domains are separated by an elastic wormlike chain peptide that can stretch under tension and is flanked by FRET donor and acceptor fluorophores (mTFP1 and venus, respectively). Tension-dependent deformation of this molecule alters the FRET signal in a graded and dynamic way, enabling visualization of tension across vinculin within individual FAs throughout the cell.

In this study, we combine this VinTS with femtosecond laser nanosurgery to determine how single SFs distribute their tensile loads across vinculin molecules within FAs. We find that while compromise of a single SF leads to overall reductions in vinculin tension, it surprisingly does not do so in a spatially or temporally uniform fashion. Specifically, we find that incision of a single SF decreases vinculin tension within some FAs while increasing it on others, and that these changes depend strongly on the directional alignment of the SF and FA. Moreover, individual FAs unexpectedly undergo highly dynamic transitions between vinculin tension-enhanced and tension-reduced states. These findings differ significantly for central versus peripheral SFs and, if reflective of tension on the entire FA, may explain the dramatic difference in how each SF population contributes to cell shape stability.

Results

Mapping tension distributions of single stress fibers

To determine how individual SFs transmit and distribute tensile loads across molecular mechanosensors within FAs, we introduced a vinculin tension sensor (VinTS) to U373 MG human glioblastoma cells stably transduced with mCherry Lifeact (Tanner et al., 2010), severed single stress fibers with femtosecond laser nanosurgery (Kumar et al., 2006; Tanner et al.,

2010) and tracked the resulting evolution of the mCherry and VinTS donor and FRET fluorescence intensities (Fig. 1). Consistent with our previous studies, SF irradiation led to retraction of the severed ends of the targeted SF (top row), and inspection of the donor and FRET intensity (middle rows) revealed that the VinTS localizes to FAs as expected. Because the FRET intensity also depends on factors unrelated to donor–acceptor separation (Chang and Mycek, 2012; Chang et al., 2007; Chang et al., 2009; Zhong et al., 2007), such as the amount of localized VinTS, we created FRET ratio maps in which we masked the FRET intensity to show only FAs and normalized this intensity by the donor intensity (bottom row). In these maps, an increasing FRET ratio corresponds to an increasing FRET signal (actual degree of energy transfer) or decreasing tension, which can in turn be tracked on an FA-by-FA basis. These FRET ratio maps show that, vinculin tension changes were not restricted to FAs in direct contact with the targeted SFs as we had expected but rather were delocalized throughout the entire cell. While some FAs exhibited significant vinculin tension reduction (increased FRET ratio), other FAs did not.

Correlating FRET response with contractile activity and cell–ECM traction

The VinTS FRET sensor reads out tension-induced strain across the vinculin molecule, which motivated us to investigate the sensitivity of the FRET signal to wholesale reductions in cellular contractile force and the predictive value of these molecular strain changes for traction stresses associated with the entire FA. To first determine if VinTS FRET signals change in expected ways following attenuation of contractile signals known to enhance cellular traction force, we measured total VinTS FRET ratios following modest pharmacological inhibition of the myosin activators ROCK (Y-27632) and MLCK (ML-7). These

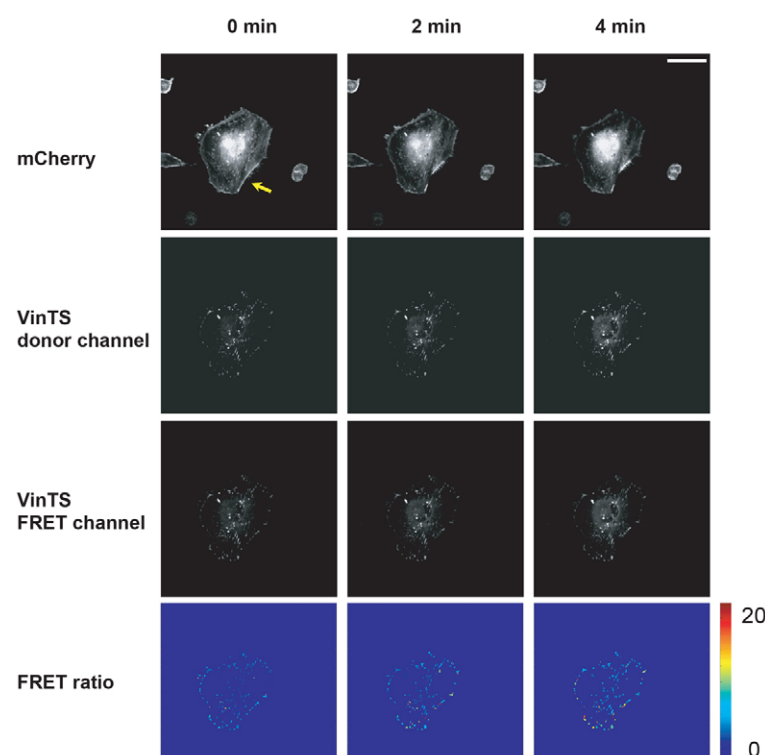


Fig. 1. Mapping tension distributions of single stress fibers. The panels depict representative mCherry-Lifeact (top row), vinculin tension sensor (VinTS) donor (second row), VinTS FRET (third row), and FRET ratio (bottom row) images immediately before (0 min) and after (2 min and 4 min) laser ablation. The SF ablation site is indicated by the arrow in the mCherry image at 0 min. In the FRET ratio maps, all vinculin signal outside of the FAs depicted was masked out to facilitate analysis (see the Materials and Methods). The hotspots in the FRET ratio maps depict regions of increased FRET ratios following SF ablation, reflecting tension reduction. The contrast and brightness of all fluorescence images were optimized for clarity of presentation (see the Materials and Methods). Scale bar: 50 μ m.

treatments moderately reduced cell spread area, SF assembly, and VinTS localization to FAs without completely disassembling FAs (not shown). As expected, and as reported previously (Grashoff et al., 2010), we observed increased VinTS FRET ratio in live cells within 1 hour (supplementary material Fig. S1), illustrating a qualitative correlation between the VinTS signal and myosin-induced traction forces. To determine whether the VinTS FRET response correlates with local traction at the cell–ECM interface, we performed traction force microscopy on VinTS-expressing cells (supplementary material Fig. S2). These measurements revealed a modest inverse linear correlation between the average traction force experienced at a VinTS-positive adhesion and the average FRET ratio within that adhesion ($R^2=0.0733$, $P=0.00029$ against the null hypothesis of no correlation), with high VinTS FRET ratios uniquely associated with low-traction FAs. Importantly, however, FAs with low FRET ratios (i.e. high apparent vinculin tension) were associated with a diverse range of traction forces, even though the mean traction force for these adhesions was comparatively high. This may be a consequence of the relatively high noise floors of the two measurements (both of which are based on fluorescence readouts) or the possibility that tension transmitted to vinculin may be dissipated by other FA proteins and not always reflect whole-FA traction. We therefore conservatively chose to interpret our measurements in terms of tension across vinculin.

FA tension falls with SF disruption and depends on SF location

Because SFs generate contractile force, one would expect that disruption of a single SF would reduce the total level of tension across vinculin within all FAs throughout the cell. To test this, we severed individual SFs and measured the total FRET ratio signal across all cellular FAs as a function of time (Fig. 2), initially restricting our analysis to FAs clearly visible throughout the entire time course of the experiment ('4-Image Tracking'). As expected, the mean FRET ratio increased following SF photo-disruption, indicating a reduction in overall FA-based vinculin

tension compared to non-irradiated control cells. Given our earlier finding that central and peripheral SFs exhibit different viscoelastic properties and contribute differently to cell shape stability (Tanner et al., 2010), we reasoned that each SF subpopulation might also contribute differently to overall levels of vinculin tension within FAs. Indeed, when we segregated the data according to SF location (Fig. 2A,B), we found that peripheral SF ablation induced a much greater overall reduction in vinculin tension than central SF ablation. The dynamics of these tension changes differed between these two groups as well, with the peripheral SF FRET ratio evolving over longer time scales than the central SF FRET ratio changes. As expected, these characteristic responses were not observed in cells transfected with a control vinculin FRET sensor lacking the tail domain (supplementary material Fig. S3).

An important limitation of this analysis is that it requires that a given FA be clearly identifiable at each of the four time points of the experiment. However, the reality is that some FAs are lost to tracking because of changes in focus, the low signal-to-noise ratio, and other factors. To determine whether exclusion of these FAs artificially influenced our result, we also tracked FAs and analyzed FRET ratios in pairs of temporally consecutive images ('2-Image Tracking'), which enabled inclusion of the FAs that would have been excluded in the longer-term analysis (Fig. 2C). The FRET ratios were analyzed separately in each time interval because an FA visible in a given temporally adjacent set of images was not always visible in the preceding or subsequent set of images. For comparison, we also applied this same analysis to the set of FAs visible through all four time points (Fig. 2B). This refined analysis revealed qualitatively similar dynamics, with the cell evolving to a lower-tension steady-state upon SF disruption and peripheral SFs contributing more to this tension reduction than central SFs.

SF disruption can either increase or decrease tension across vinculin within a given FA

The previous results show that photo-disruption of an SF reduces total FA-based vinculin tension in the cell, which in turn depends

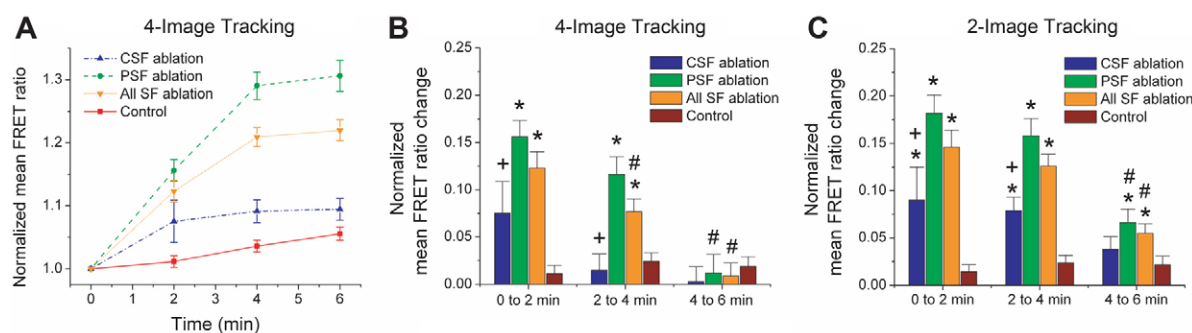


Fig. 2. SF incision reduces total tension in cellular FAs. (A) Overall mean normalized FRET ratio versus time for '4-Image Tracking', i.e. including only FAs that were clearly visualized throughout all four time points of the experiment. The FRET ratio values were normalized to the corresponding FRET ratio at time 0 min. The statistics are based on 546 focal adhesions from 17 cells for peripheral SF (PSF) ablation, 376 FAs from 10 cells for central SF (CSF) ablation, and 164 FAs from 8 cells for non-irradiated control cells. The increase in the control FRET ratio is presumably due to fluorophore photobleaching that was not fully corrected. [See supplementary material Fig. S3 for vinculin tail-less sensor (Grashoff et al., 2010) results]. (B) Changes in overall mean normalized FRET ratios across adjacent time points for the set of FAs considered in A (see the text). The FRET ratio changes were normalized to the corresponding FRET ratio at the first time point of each two-minute interval. (C) Changes in overall mean normalized FRET ratios for FAs that could be tracked across two temporally consecutive images ('2-Image Tracking'). As in B, FRET ratio changes were normalized to the corresponding FRET ratio at the first time point of each two-minute interval. The statistics are based on 681–716 FAs from 17 cells for peripheral SF ablation, 458–485 FAs from 10 cells for central SF ablation, and 226–232 FAs from 8 cells for controls. * $P<0.05$ compared with corresponding control; + $P<0.05$ for CSF vs PSF; # $P<0.05$ compared with the corresponding '0 to 2 min' group. In all cases, the data are means \pm s.e.m. and statistical comparisons were performed using two-tailed Student's *t*-tests.

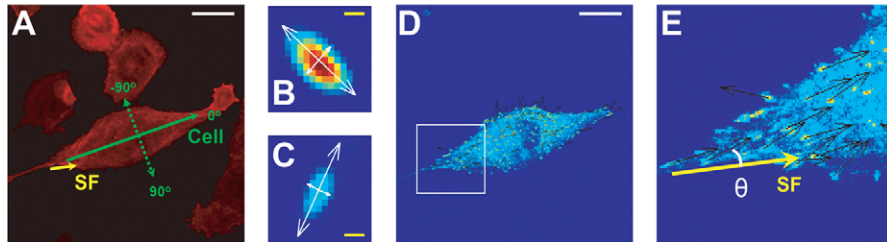


Fig. 3. Coordinate system for measuring relative orientations of SFs and FAs. (A) Schematic of coordinate system. We defined FA angles as the angles between the long axis of each FA and the axial orientations of the cell (green solid arrow) or the severed SF (yellow solid arrow). The cell-referenced angle system is also shown (dotted arrow and labels). For clarity, only the image of the SF network (mCherry-Lifeact) is shown. (B,C) Examples of FA orientations showing their long and short axes. (D) Cell with FA orientations (arrows) overlaid upon a FRET intensity image, with region enclosed by white square zoomed and shown in (E). The angle of a selected FA is illustrated as θ with the severed SF axis as the reference. The colors in (B–E) reflect arbitrary units of VinTS FRET channel fluorescence intensity. White scale bars: 50 μm ; yellow scale bars: 1 μm .

on the location of the SF. As we further considered the relationship between SF geometry and FA tension, we noted from the FRET ratio maps (Fig. 1) that the FRET signal of a given FA appeared to depend on the degree to which the FA was aligned with the severed SF. This is consistent with past observations that FAs typically align in the direction of net applied tension, which would be expected to coincide with the orientation of one or more attached SFs (Goffin et al., 2006; Tan et al., 2003). To quantify this observation, we defined an orientation angle between the severed SF and the long axis of each FA in the cell (Fig. 3A–C) and used this coordinate system to further explore the geometric distribution of SF tension (Fig. 3D,E). For control cells in which no SF was severed, we used the long axis of the cell itself as the reference, which in practice is frequently parallel to the most prominent cellular SFs.

Equipped with this coordinate system, we plotted FRET ratio changes within each individual FA as a function of its angle of orientation to the severed SF (Fig. 4A–C, binned into box-and-whisker plots). Here, each data point represents the FRET ratio change for a single FA, with points falling above and below the horizontal axis (zero normalized FRET ratio change) experiencing reduced and enhanced vinculin tension, respectively. We thus defined FAs with FRET ratio values higher than the 95th percentile and lower than the 5th percentile of the corresponding control distribution to be tension-reduced and tension-enhanced FAs, respectively (supplementary material Fig. S4; Table S1; abbreviated as TR and TE, respectively). Approximately 26% of all FAs fell within the tension-reduced category, and this subpopulation of FAs was not restricted to the FAs projected to be in direct contact with the ablated SFs (see below and Fig. 4E for quantitative analysis). Surprisingly, $\sim 12\%$ of FAs fell within the tension-enhanced category, reflecting a population of FAs experiencing *increased* tension upon SF ablation. In other words, even though ablation of a single SF reduces overall vinculin tension in FAs throughout the cell (Fig. 2), these tension reductions reflect the net result of a complex tension redistribution in which tension across vinculin falls in some FAs and increases in others.

SFs distribute tension in a spatially non-uniform fashion

To understand the dependence of vinculin tension reduction and enhancement on FA orientation, we considered the angular distributions of the FRET ratio changes from one time point to

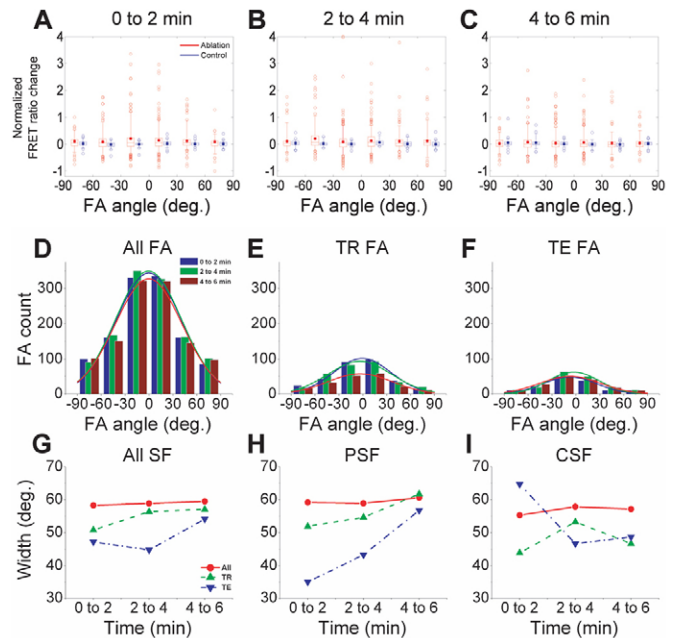


Fig. 4. SFs distribute tension to FAs in an angle-dependent manner. (A–C) Distributions of normalized FRET ratio changes in individual FAs following SF ablation. The FRET ratio changes were calculated from 2-image FA tracking (Fig. 2C) over the indicated time intervals, and then plotted as a function of the angle between FA long axis and the reference axis (SF axis for ablated cells and cell long axis for non-ablated controls, as shown in Fig. 3A). The corresponding central and peripheral SF-ablation subpopulations are shown in supplementary material Fig. S8. The FRET ratio changes were normalized to the corresponding FRET ratio at the first time point of each two-minute interval. The horizontal box lines indicate 25th, 50th and 75th percentiles, the whisker ends indicate 5th and 95th percentiles, and the solid dots indicate mean values. Each data point represents one FA. (D–F). Time-dependent histograms of angles between FA and SF orientations for (D) all FAs, (E) tension-reduced (TR) FAs, and (F) tension-enhanced (TE) FAs. The curves are the corresponding Gaussian curve fits. The histograms for central and peripheral SF-ablation subpopulations are shown in supplementary material Fig. S9. (G–I). Breadth of tension distributions as a function of time and SF location. (G) Gaussian widths for all FAs, with the red, green, and blue curves (all, tension-reduced, and tension-enhanced) corresponding to the Gaussian fits shown in D–F, respectively. (H,I) Gaussian widths for (H) peripheral SF (PSF) and (I) central SF (CSF) subpopulations.

another (Fig. 4A–C). At the earliest time interval following SF ablation (Fig. 4A), the distribution exhibited a broad peak around 0° , indicating that these tension changes were preferentially concentrated in FAs co-aligned with the SF, which are most likely to be found near the ends of the SF. The significant breadth of the peak further indicates that these tension changes are also delocalized across FAs located throughout the cell, which was evident from the FRET ratio maps (Fig. 1). Over time (Fig. 4B,C), the angle-dependence of the curve dissipates, indicating achievement of a new tensile steady-state. Importantly, this feature did not disappear following normalization of distributions to the maximal amplitude, indicating that the zero-angle FRET ratio peak was not simply a sampling artifact associated with the high number of FAs found at this angle (supplementary material Fig. S5) (Moore and McCabe, 2002).

To further quantify and understand the dynamics of this angle specificity, we asked whether FAs exhibiting strong changes in vinculin tension are preferentially enriched in specific orientations relative to the ablated SF. To do this, we constructed histograms of FA number as a function of orientation angle for all FAs, vinculin tension-reduced FAs and vinculin tension-enhanced FAs (Fig. 4D–F, with tension-reduced FAs and tension-enhanced FAs defined as described above and as depicted in supplementary material Fig. S4 and Table S1). Here, the total FA histogram (Fig. 4D) serves as a reference, where distributions narrower or wider than this indicate an angle-specificity close to or away from the targeted SF orientation, respectively. Analysis of this angle-specificity, which we quantified as the width of the corresponding Gaussian fit (Fig. 4G), revealed two important features of the tension-reduced and tension-enhanced populations. First, the angle-specificities of both populations were significantly more dynamic than the overall FA population, which displayed a relatively constant distribution width throughout the time course (Fig. 4G, circles). This constant distribution also illustrates that FA orientations were relatively stable throughout the time course, with minimal rotation. Second, the magnitude of the distribution widths were significantly narrower for the tension-enhanced and tension-reduced populations, particularly at early time points, indicating that both subpopulations are most likely to be found in FAs co-aligned with the SF and presumably found near SF ends.

Central and peripheral SFs produce different vinculin tension distributions

As mentioned earlier, central and peripheral SFs contribute differently to cell shape stability (Tanner et al., 2010), which suggests that these two SF subpopulations spatially distribute tension in distinct ways and that this might be reflected in differential vinculin tension delocalization following ablation of each subpopulation of SFs. To test this hypothesis, we plotted the distribution widths of these two subpopulations separately (Fig. 4H,I). Within 2 min of peripheral SF ablation (Fig. 4H), tension-reduced and especially tension-enhanced FAs were distributed much more narrowly in angular orientation than all FAs. This indicates that the majority of vinculin tension changes, particularly enhancements, occurred in FAs oriented along the axis of the targeted SF following photo-disruption. This strongly contrasted with the angle specificity dynamics following central SF ablation (Fig. 4I), in which tension-enhanced FAs (inverted triangles) were initially distributed much more broadly than either the total (circles) or tension-reduced FA (upright triangles) populations. We reasoned that the qualitatively symmetric but opposite kinetics displayed by vinculin within tension-enhanced and tension-reduced FA populations might be due to exchange of tension between different subsets of FAs, potentially mediated by physical connections within the cellular SF network.

Vinculin undergoes highly dynamic tension transitions following SF ablation

If tension indeed can be transferred between FAs through the SF network following SF ablation, one would expect to observe time dependent changes in the tensile state of vinculin within individual FAs. To explore this, we followed the FRET ratio for individual FAs following SF ablation and mapped the trajectory of each FA through the three tensile states (non-tension-reduced/tension-enhanced, tension-reduced, and tension-enhanced) over the three time intervals examined above. (Fig. 5; in these representations, the intensity of the color reflects the number of FAs in a given category for a given time interval, and the width of the transition line reflects the number of FAs transitioning between two specific states from one time interval to another). As expected from our earlier analysis (Fig. 4A), most FAs were in the non-tension-reduced/tension-enhanced category and remained so for the entire observation period. However, the

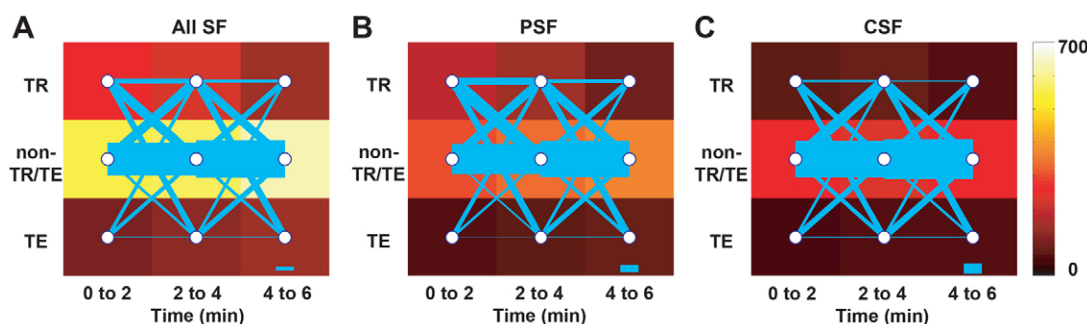


Fig. 5. FAs undergo dynamic tension transitions following SF ablation. Tension state transition plots for (A) all SFs, (B) peripheral SF (PSF), and (C) central SF (CSF) subpopulations. FAs were analyzed from 4-image tracking data depicted in Fig. 2A,B. In these diagrams, each of the nine tiles represents the category into which a given FA falls [tension-reduced (TR), tension-enhanced (TE), non-tension-reduced/tension-enhanced] for a given time interval, with the color representing the number of FAs (see scale on right-hand side). The lines between temporally adjacent tiles reflect FAs transitioning from one state to another, with the thickness of each line indicating the number of FAs undergoing that particular transition (which can include remaining in the same state). Scale bar thickness: 50 FAs (note variation of scale between panels).

smaller subset of FAs in the tension-enhanced and tension-reduced states predominantly underwent highly dynamic transitions between the three states. In cases where non-tension-reduced/tension-enhanced FAs exhibited these dynamics, more transitioned from the non-tension-reduced/tension-enhanced state to the tension-reduced than to the tension-enhanced state, consistent with our earlier finding that SF ablation induces an overall tension reduction (Fig. 2A).

Moreover, for the peripheral SF population (Fig. 5B), the number of tension-reduced FAs continuously decreased, again in agreement with our previous finding (Fig. 2A), while those of tension-enhanced FAs, and non-tension-reduced/tension-enhanced FAs continuously increased (indicated by the color scale), despite the fact that ablation of a peripheral SF leads to overall reductions in tension (Fig. 2A). A quantitative analysis of these tensional transitions indicated that the most significant difference in central and peripheral SF subpopulations (Fig. 5B,C) lay in the percentage of adhesions that begin in the tension-reduced state at one time interval and then transition to the tension-enhanced state in the subsequent time interval (43.5% and 43.9% for central SFs for the earlier and later transitions versus 25.0% and 35.4% respectively for peripheral SFs). This could potentially be explained by greater mechanical 'communication' between FAs following central SF photo-disruption, which would also explain why the numbers of both tension-reduced and tension-enhanced FAs were more stable for the central SF population (Fig. 5C) than the peripheral SF

population. In other words, tension dissipated by compromise of a central SF is redistributed to vinculin within a broader complement of FAs than for peripheral FAs, where comparatively few tensional transitions are observed.

To gain insight into the relationship between these transitions and myosin-dependent contractile activity, we pharmacologically pre-treated cells with the MLCK inhibitor ML-7 and the ROCK inhibitor Y-27632 prior to SF ablation (supplementary material Fig. S6). While some trends were preserved (e.g. decreasing numbers of tension-reduced FAs but increasing numbers of tension-enhanced and non-tension-reduced/tension-enhanced FAs along the time course; see 1st column, supplementary material Fig. S6), both treatments enhanced the total number of transitions following SF ablation, suggesting that mechanical communication between FAs is sensitive to motor activity within the actomyosin cytoskeleton.

To conceptually unify all of these findings, we devised a structural model in which central SFs are more physically interconnected and mutually reinforced than peripheral SFs due to the presence of transverse actomyosin structures that link central SFs into a cohesive network. This model is supported by confocal imaging, which reveals many cross-connections between central SFs but comparatively few between peripheral SFs (Fig. 6A–D; supplementary material Fig. S7 illustrates our ability to sever single central SFs). In our model, these lateral connections explain the differences in tension redistribution and shape stability associated with compromise of central and

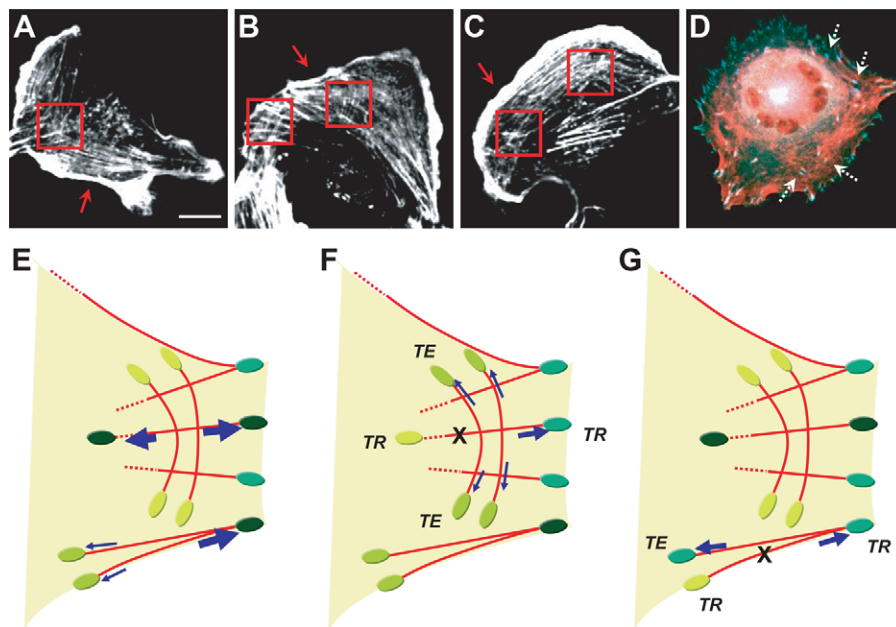


Fig. 6. Structural model of SF tension distribution across cellular FAs. (A–C) Confocal fluorescence images depicting actin cytoskeleton (phalloidin). Red boxes highlight regions where lateral interconnections between central SFs are clearly visible. Arrows indicate peripheral SFs, which exhibit these lateral connections to a much lesser extent. (D) Live-cell image illustrating actomyosin cytoskeletal structure (mCherry-Lifeact, red) and FAs [overlaid VinTS donor (blue) and FRET (green) channels]. White dotted arrows indicate FAs that are associated with the transverse actomyosin structures. Scale bar: 20 μ m. (E–G) A simplified model for tension re-distribution after (F) central and (G) peripheral SF photo-disruption, following disruption of the mechanical equilibrium depicted in (E). FAs are represented by green ovals, with a darker green color indicating higher tension experienced by that FA. Blue arrows represent the involved force vectors along SFs, with stronger force reflected by thicker arrows. The red solid or dashed lines depict the SFs. The ablation site is indicated by an 'X'. In this model, the interconnected central SFs re-direct tension to a broader array of FAs with a diversity of cellular locations and orientations, which preserves cell shape after SF ablation. Conversely, peripheral SFs, which are not as structurally coupled into the total SF network, distribute dissipated tension to a narrower segment of cellular FAs with similar orientations. Thus, peripheral SF disruption is more likely to trigger FA rupture and cellular contraction. TE, tension-enhanced FA; TR, tension-reduced FA.

peripheral SFs. We specifically speculate that these lateral connections provide physical conduits for the dissipation of released tension to vinculin mechanosensors localized with multiple FAs (Fig. 6E–G). If the tensile state of vinculin reflects tension in the entire FA (an assumption discussed at length below), disruption of a central SF leads to robust redistribution of the released tension to FAs throughout the entire cell and thus is not strongly accompanied by compromise of cell shape, whereas disruption of a peripheral SF produces a relatively narrow spatial redistribution of tension and thus is accompanied by FA rupture and catastrophic collapse of cell shape. In both cases, the frequency of these transitions increases in the setting of myosin inhibition. While the mechanism of this myosin dependence remains unclear, one possibility is that the reduced actomyosin sliding velocity associated with myosin inhibition reduces viscous dissipation of tension upon SF retraction (Besser and Schwarz, 2007; Colombelli et al., 2009), which in turn frees this tension to be redistributed throughout the SF network.

Discussion

In this study, we have elucidated how tensile forces generated by single SFs are temporally and spatially distributed to vinculin mechanosensors located within cell–matrix adhesions by using femtosecond laser nanosurgery and a FRET-based tension sensor. Our results demonstrate that following SF photo-disruption, vinculin localized to FAs throughout the cell can undergo both tension reduction and enhancement. The magnitude of vinculin tension change in an FA depends strongly on the co-alignment of the FA and disrupted SF, and the spatial and temporal redistribution of vinculin tension following incision differs dramatically for central and peripheral SFs. Specifically, incision of a central SF is accompanied by a broad redistribution of vinculin tension within FAs throughout the cell and a highly dynamic set of tension transitions, which is consistent with the observation that cell structure is relatively stable to photo-disruption of this SF subpopulation.

It is important to note that our measurements are based on the use of a sensor that tracks tension borne by a specific FA molecule, vinculin, which populates the FA in the context of both endogenous vinculin and the multitude of other proteins that localize to FAs (Kanchanawong et al., 2010). It remains unclear whether this readout may be used as a surrogate for tension within the entire FA or traction force generated by an FA against the ECM. Several lines of evidence support a correlation between these three quantities: First, pharmacologic inhibition of contractility is accompanied by an increase in VinTS FRET ratio across the whole cell (supplementary material Fig. S1). Second, the pattern in which SFs distribute vinculin tension in this study qualitatively resembles the pattern with which SFs are known to distribute traction forces (Kumar et al., 2006). Third, we observe a gross correlation between VinTS FRET signal and traction force for a given adhesion (supplementary material Fig. S2). Nonetheless, this last correlation is a comparatively modest one, with most FAs generating small VinTS FRET signals and being associated with a broad range of traction force values. As discussed earlier, this may be a consequence of the relatively high noise floor in the FRET measurements (leading to overrepresentation of low-FRET adhesions) or the possibility that changes in sensor tension do not always reflect the tensile state of the whole adhesion. This second notion is consistent with

the very real possibility that tension across vinculin is highly regulated within FAs and may vary in non-intuitive ways with overall FA tension, e.g. through altered protein–protein interactions or maturation state. We do not regard our study as definitively resolving this question either way, and we suspect that revisiting these measurements with higher-resolution TFM measurements, improved FRET pairs (Lam et al., 2012), and analogous sensors based on other FA proteins should help clarify this issue.

Nonetheless, it is valuable to consider the implications for cellular structure and mechanics if these measurements indeed reflect alterations in whole-FA tension and cell–ECM traction. Our findings would challenge the common notion that the tension generated by a given SF is concentrated primarily near its points of attachment. More generally, our finding that stress fiber network connectivity plays a role in intracellular force redistribution supports and lends direct mechanistic insight into the emerging idea that specific cytoskeletal elements can rapidly transmit mechanical information across specific positions within the cell. For example, application of stress to integrin-based adhesions can deform organelles (Hu et al., 2005) and activate mechanotransductive signals at distal cellular locations less than one second after imposition of force, in contrast to canonical receptor–ligand signaling (Na et al., 2008; Wang et al., 2009). Our findings hint that the physical ‘wiring’ of the SF network may directly shape the speed and directionality of this transmission process, with different routes channeling varying degrees of tension to different adhesive nodes at the cell–matrix interface.

An important feature of our model (again, assuming that vinculin tension reflects whole-FA tension and traction) is that lateral connections between SFs provide a mechanism to broadly distribute tension released from a severed SF and thus maintain cellular structural integrity. This may be placed in context of past studies of SF network structure and its possible role in cellular tension transmission (Hotulainen and Lappalainen, 2006; Hwang and Barakat, 2012; Rossier et al., 2010; Tondon et al., 2012). In particular, SFs have been broadly classified into three different categories: transverse arcs, dorsal SFs, and ventral SFs. Transverse arcs are typically oriented normally to the anteroposterior axis of the cell, physically couple and may later evolve into ventral stress fibers, and do not closely associate with FAs. Our model would predict that these transverse arcs function to mechanically couple other SFs and distribute load. Interestingly, the transverse structures in the cells considered here sometimes do appear to anchor into FAs (Fig. 6D), suggesting that these SFs may be in the process of evolving into ventral SFs. High-resolution live-cell time-lapse imaging on SF assembly and evolution in these experiments may lend insight into this possibility. Moreover, recent modeling efforts strongly support a role for SFs aligned orthogonally to the direction of force application in the rapid and robust transmission of force across the cell (Hwang and Barakat, 2012); in our system, the applied force is the tension released upon stress fiber incision, and the orthogonal population of SFs is the transverse SFs. Thus, different SF subpopulations may play diverse and previously unappreciated mechanical roles in maintaining shape stability through the differential transmission of tensile information. More specifically for our studies, central SF photo-disruption causes spontaneous vinculin tension enhancement in FAs with various orientations due to force transmission through the

inter-connection of the targeted SF and the transverse SFs (Fig. 6E,F), which facilitates tension transmission to a broader area and hence dissipates the mechanical disturbance more quickly. Therefore, the high resistance of the cell to structural changes following central SF ablation relative to peripheral SF ablation (Tanner et al., 2010) can be attributed not only to differences in initial tension (Fig. 2) but also to differences in the physical connectivity of those SFs to the transverse SF network.

Another unexpected and very interesting discovery revealed by our studies is the highly dynamic transitions in vinculin tension enhancement/reduction states following SF ablation (Fig. 5). If our FRET measurements reflect whole-FA tension and traction changes, this would provide additional molecular-scale evidence that FAs mutually transmit force to one another, potentially as part of a shape-stabilization strategy. Importantly, while both peripheral and central SFs exhibit these transitions, peripheral SFs do so to a much lesser extent, and appear to concentrate those tension changes in a more localized pool of FAs. Somewhat unexpectedly, ML-7 and Y-27632 pre-treatments of cells increased the number of transitions. We hypothesize that this effect is related to the viscous drag of actin–myosin sliding, as described in previous mechanical models of SFs (Besser and Schwarz, 2007; Colombelli et al., 2009). Specifically, when SFs are severed in the absence of myosin inhibition, sliding and SF retraction occur rapidly, and the resulting viscous drag dissipates tensile force that would otherwise be transmissible to other SFs and adhesions. When myosin is inhibited, sliding velocity and viscous drag fall, and the dissipated tension is more easily transmitted throughout the SF network. Importantly, this does not imply that the magnitude of transmitted tension is greater upon myosin inhibition, only that the number of transition events increases. Related to (and consistent with) this framework, recent experimental observations (Colombelli et al., 2009) and numerical simulations (Besser et al., 2011) of post-ablation SF dynamics reveal damped oscillations in the ends and interior of the severed fiber, which in turn derives from the competing influences of SF elasticity and frictional coupling to the cytoplasm. While the technical demands of our combined ablation/FRET measurements did not allow us to directly visualize these oscillations in our system, it is conceivable that these oscillations may be contributing to the vinculin tension transitions we observe at individual FAs. The plausibility of this hypothesis could be tested in the future via construction of multiscale models that incorporate SF viscoelastic properties, SF network architecture, and FA-based mechanosensing, as well as experimental studies with myosin mutants with defined mechanochemical alterations.

Our studies also raise a number of important open questions for future investigation. The first is the overall utility of tension across vinculin as a readout of whole-FA tension and traction, which as described above could be addressed with higher-resolution measurements and a broader palette of optical sensors. Second, it would be informative to determine how SF tension distributions depend on the organization and anisotropy of the overall SF network, which can now be controlled to some extent by micropatterning (Ronchi et al., 2012; Théry, 2010). By dictating FA geometry and thus the length and orientation of intervening SFs, such measurements may also enable elucidation of length–tension relationships for SFs, which have thus far been difficult to clearly measure in living cells. These methods may also enable more precise control of SF thickness, which could

potentially make it possible to understand whether the thickness can alter the roles of SFs at different locations. Finally, by combining femtosecond laser ablation with FRET-based molecular biosensors, this study introduces a significant methodological advance that may be broadly applicable for quantitatively studying mechanochemical coupling between load-bearing cytoskeletal elements and the signaling complexes into which they attach, such as insertion of actin bundles into cadherin complexes (Borghi et al., 2012; le Duc et al., 2010). This strategy may also potentially be generalized to analogous interactions between load-bearing elements in tissue (e.g. ECM fibers) and their cognate sites of anchorage (e.g. integrin-based adhesions). Clearly, progress in this area will be greatly aided by continued methodological advances in photoablation technology and the development of new optogenetic force sensors.

Materials and Methods

Cell culture, transduction, and transient transfection

U373 MG human glioblastoma cells were stably transduced with mCherry-Lifeact (Tanner et al., 2010) and then transiently transfected with a previously described vinculin tension sensor (VinTS) (Grashoff et al., 2010) (Addgene, Plasmid ID#: 26019) using polyethyleneimine-based transfection (Tinsley et al., 2004; Zhang et al., 2004). The transfected cells were plated on 35 mm 1.5 coverslip-bottomed dishes (0.16–0.19 mm, MatTek Corporation, Ashland, MA) coated with fibronectin at a density of 10 $\mu\text{g}/\text{cm}^2$, and then cultured at 37°C supplied with 5% CO_2 until imaging. Cultures were imaged at low (~40%) confluence to minimize or eliminate cell–cell contacts that may play a role in cellular responses after SF photo-disruption.

Confocal imaging and photo-disruption of single SFs

All mCherry-Lifeact imaging, VinTS imaging, and SF photo-disruption experiments were performed on a Zeiss LSM 510 Meta confocal microscope equipped with a MaiTai Ti:sapphire femtosecond laser (Spectra Physics, Newport Beach, CA) based on previously published protocols (Kumar et al., 2006; Tanner et al., 2010). 35 mm dishes with fluorescent live cells were placed on a plate heater (Warner Instruments) set at 37°C during imaging. mCherry-Lifeact images (excitation: 543 nm, emission: 565–615 nm), VinTS FRET channel images (excitation: 458 nm, emission: 533–587 nm), and VinTS donor channel images (excitation: 458 nm, emission: 469–501 nm) were obtained by one-photon confocal imaging with a 40 \times water-dipping objective (NA=0.8). For SF photo-disruption, the femtosecond laser was used at 770 nm for one iteration, resulting in energy deposition of 1–2 nJ on a single stress fiber. All images were acquired with 512 \times 512 pixels and pixel size=0.41 μm . For presentation purposes, the contrast and brightness of fluorescence images were optimized using ImageJ.

FRET ratio mapping

VinTS FRET and donor channel images were first background-subtracted and corrected for photobleaching, which was implemented by taking the overall fluorescence intensity of each image excluding the background and the identified FA regions (see below), and using this overall intensity value to normalize each image to its corresponding image at the first time point. Note that this approach assumes that the majority of cytoplasmic VinTS is subject to photobleaching but experiences no dramatic tension change. FA FRET ratio maps were then generated by taking the ratio of the FRET channel signals to the VinTS donor channel signals, using the same identified FA masks (see below).

Traction force microscopy

Traction force microscopy was performed according to our previous studies (MacKay et al., 2012; Sen et al., 2009) using fibronectin-coated 30 kPa polyacrylamide gels embedded with far-red or infrared beads (Life Technologies, Cat. No.: F8816, F8807, and F8799). Traction maps were first obtained using Fourier transform traction cytometry (Butler et al., 2002) and then subjected to an FA mask in order to isolate traction forces at adhesions [adapted from (Gardel et al., 2008; Plotnikov et al., 2012; Stricker et al., 2011; Stricker et al., 2010)].

Single FA identification, tracking, and morphometric/orientational analysis

FAs in VinTS fluorescence intensity images were identified using the previously described ‘water algorithm’ (Grashoff et al., 2010; Zamir et al., 1999) with merger size=20 pixels (3.36 μm^2) and FA reject size=5 pixels (0.84 μm^2). Briefly, after background subtraction, all pixels were sorted from highest to lowest intensity, and each pixel was inspected one-by-one to determine if it belonged to a certain FA. If

the pixel was not in contact (8-point connectivity) with any previous pixels, it would be assigned to a new FA; otherwise, if the pixel was in contact with only one previously assigned FA, it would be assigned to that FA. When a pixel was in contact with more than one previously assigned FAs, these FAs would be merged to form a new FA if the size of at least one of these FAs was less than the merger size; otherwise, the pixel would be assigned to the brightest FA, with no merger. This process continued until each pixel was assigned to an FA, and then all FAs with sizes less than the reject size would be removed.

After FA identification, images were shifted, if necessary, relative to the image at the first time point to remove any unexpected xy-plane displacement and/or drifting during imaging. Tracking was then applied to the identified FAs using a previously reported IDL particle tracking method (Cheezum et al., 2001; Crocker and Grier, 1996). In our FA tracking, the maximum displacement was set to 10 pixels (4.1 μm) and no disappearing of FA was allowed at any time point.

FA orientation was then determined with a gradient-based structure tensor (also known as the second-moment matrix) method (Zamir et al., 1999) for those successfully identified and tracked FAs. After determining the two ellipse axes of an FA (Fig. 3B,C) the orientation of the FA was assigned to be the longer axis with the upward direction (the vector in the 1st or 2nd quadrants in the Cartesian coordinate system). The angle of orientation was then reassigned to be within 90° and -90° relative to either the severed SF or the cell orientation (see below), both in the upward direction as well (Fig. 3A).

For cell orientation (long axis) determination, we first considered all vectors in 1° increments in the upward (positive y) direction passing through the cell center of mass, and then calculated the sum of squares of the shortest distances of all pixels in the cell to the vector. The orientation was determined to be the vector that produced the minimum sum.

Author contributions

C.-W.C. was responsible for conception and design, collection and assembly of data, data analysis and interpretation, and manuscript writing. S.K. was responsible for obtaining financial support, conception and design, data analysis and interpretation, manuscript writing, and final approval of manuscript.

Funding

This work was supported by the National Institutes of Health [Director's New Innovator Award 1DP2OD004213 and Physical Sciences–Oncology Center Award 1U54CA143836 to S.K.]; and the National Science Foundation [CAREER Award CMMI 1055965 to S.K.]. Deposited in PMC for release after 12 months.

Supplementary material available online at
<http://jcs.biologists.org/lookup/suppl/doi:10.1242/jcs.119032/-/DC1>

References

- Besser, A. and Schwarz, U. S. (2007). Coupling biochemistry and mechanics in cell adhesion: a model for inhomogeneous stress fiber contraction. *New J. Phys.* **9**, 425.
- Besser, A., Colombelli, J., Stelzer, E. H. and Schwarz, U. S. (2011). Viscoelastic response of contractile filament bundles. *Phys. Rev. E Stat. Nonlin. Soft Matter Phys.* **83**, 051902.
- Borghi, N., Sorokina, M., Shcherbakova, O. G., Weis, W. I., Pruitt, B. L., Nelson, W. J. and Dunn, A. R. (2012). E-cadherin is under constitutive actomyosin-generated tension that is increased at cell-cell contacts upon externally applied stretch. *Proc. Natl. Acad. Sci. USA* **109**, 12568–12573.
- Butler, J. P., Tolić-Nørrelykke, I. M., Fabry, B. and Fredberg, J. J. (2002). Traction fields, moments, and strain energy that cells exert on their surroundings. *Am. J. Physiol.* **282**, C595–C605.
- Chang, C. W. and Mycek, M. A. (2012). Quantitative molecular imaging in living cells via FLIM. In *Reviews in Fluorescence* (ed. C. D. Geddes), pp. 173–198. New York, NY: Springer.
- Chang, C. W., Sud, D. and Mycek, M. A. (2007). Fluorescence lifetime imaging microscopy. *Methods Cell Biol.* **81**, 495–524.
- Chang, C. W., Wu, M., Merajver, S. D. and Mycek, M. A. (2009). Physiological fluorescence lifetime imaging microscopy improves Förster resonance energy transfer detection in living cells. *J. Biomed. Opt.* **14**, 060502.
- Cheezum, M. K., Walker, W. F. and Guilford, W. H. (2001). Quantitative comparison of algorithms for tracking single fluorescent particles. *Biophys. J.* **81**, 2378–2388.
- Cohen, D. M., Kutscher, B., Chen, H., Murphy, D. B. and Craig, S. W. (2006). A conformational switch in vinculin drives formation and dynamics of a talin–vinculin complex at focal adhesions. *J. Biol. Chem.* **281**, 16006–16015.
- Colombelli, J., Pepperkok, R., Stelzer, E. H. K. and Reynaud, E. G. (2006). [Laser nanosurgery in cell biology]. *Med. Sci. (Paris)* **22**, 651–658.
- Colombelli, J., Besser, A., Kress, H., Reynaud, E. G., Girard, P., Caussinus, E., Haselmann, U., Small, J. V., Schwarz, U. S. and Stelzer, E. H. (2009). Mechanosensing in actin stress fibers revealed by a close correlation between force and protein localization. *J. Cell Sci.* **122**, 1665–1679.
- Crocker, J. C. and Grier, D. G. (1996). Methods of digital video microscopy for colloidal studies. *J. Colloid Interface Sci.* **179**, 298–310.
- Deguchi, S., Ohashi, T. and Sato, M. (2006). Tensile properties of single stress fibers isolated from cultured vascular smooth muscle cells. *J. Biomech.* **39**, 2603–2610.
- Dupont, S., Morsut, L., Aragona, M., Enzo, E., Giulitti, S., Cordenonsi, M., Zanconato, F., Le Digabel, J., Forcato, M., Bicciato, S. et al. (2011). Role of YAP/TAZ in mechanotransduction. *Nature* **474**, 179–183.
- Etienne-Manneville, S. and Hall, A. (2002). Rho GTPases in cell biology. *Nature* **420**, 629–635.
- Fu, J., Wang, Y. K., Yang, M. T., Desai, R. A., Yu, X., Liu, Z. and Chen, C. S. (2010). Mechanical regulation of cell function with geometrically modulated elastomeric substrates. *Nat. Methods* **7**, 733–736.
- Gardel, M. L., Sabass, B., Ji, L., Danuser, G., Schwarz, U. S. and Waterman, C. M. (2008). Traction stress in focal adhesions correlates biphasically with actin retrograde flow speed. *J. Cell Biol.* **183**, 999–1005.
- Goffin, J. M., Pittet, P., Csucs, G., Lussi, J. W., Meister, J. J. and Hinz, B. (2006). Focal adhesion size controls tension-dependent recruitment of alpha-smooth muscle actin to stress fibers. *J. Cell Biol.* **172**, 259–268.
- Grashoff, C., Hoffman, B. D., Brenner, M. D., Zhou, R., Parsons, M., Yang, M. T., McLean, M. A., Sligar, S. G., Chen, C. S., Ha, T. et al. (2010). Measuring mechanical tension across vinculin reveals regulation of focal adhesion dynamics. *Nature* **466**, 263–266.
- Hotulainen, P. and Lappalainen, P. (2006). Stress fibers are generated by two distinct actin assembly mechanisms in motile cells. *J. Cell Biol.* **173**, 383–394.
- Hu, S. H., Chen, J. X., Butler, J. P. and Wang, N. (2005). Prestress mediates force propagation into the nucleus. *Biochem. Biophys. Res. Commun.* **329**, 423–428.
- Hwang, Y. and Barakat, A. I. (2012). Dynamics of mechanical signal transmission through prestressed stress fibers. *PLoS ONE* **7**, e35343.
- Hytönen, V. P. and Vogel, V. (2008). How force might activate talin's vinculin binding sites: SMD reveals a structural mechanism. *PLOS Comput. Biol.* **4**, e24.
- Kanchanawong, P., Shtengel, G., Pasapera, A. M., Ramko, E. B., Davidson, M. W., Hess, H. F. and Waterman, C. M. (2010). Nanoscale architecture of integrin-based cell adhesions. *Nature* **468**, 580–584.
- Katoh, K., Kano, Y. and Ookawara, S. (2007). Rho-kinase dependent organization of stress fibers and focal adhesions in cultured fibroblasts. *Genes Cells* **12**, 623–638.
- Katoh, K., Kano, Y. and Noda, Y. (2011). Rho-associated kinase-dependent contraction of stress fibres and the organization of focal adhesions. *J. R. Soc. Interface* **8**, 305–311.
- Kumar, S., Maxwell, I. Z., Heisterkamp, A., Polte, T. R., Lele, T. P., Salanga, M., Mazur, E. and Ingber, D. E. (2006). Viscoelastic retraction of single living stress fibers and its impact on cell shape, cytoskeletal organization, and extracellular matrix mechanics. *Biophys. J.* **90**, 3762–3773.
- Lam, A. J., St-Pierre, F., Gong, Y., Marshall, J. D., Cranfill, P. J., Baird, M. A., McKeown, M. R., Wiedenmann, J., Davidson, M. W., Schnitzer, M. J. et al. (2012). Improving FRET dynamic range with bright green and red fluorescent proteins. *Nat. Methods* **9**, 1005–1012.
- le Duc, Q., Shi, Q. M., Blonk, I., Sonnenberg, A., Wang, N., Leckband, D. and de Rooij, J. (2010). Vinculin potentiates E-cadherin mechanosensing and is recruited to actin-anchored sites within adherens junctions in a myosin II-dependent manner. *J. Cell Biol.* **189**, 1107–1115.
- Lele, T. P., Pendse, J., Kumar, S., Salanga, M., Karavitis, J. and Ingber, D. E. (2006). Mechanical forces alter zyxin unbinding kinetics within focal adhesions of living cells. *J. Cell. Physiol.* **207**, 187–194.
- Levental, K. R., Yu, H., Kass, L., Lakins, J. N., Egeblad, M., Erler, J. T., Fong, S. F., Csiszar, K., Giaccia, A., Weninger, W. et al. (2009). Matrix crosslinking forces tumor progression by enhancing integrin signaling. *Cell* **139**, 891–906.
- MacKay, J. L., Keung, A. J. and Kumar, S. (2012). A genetic strategy for the dynamic and graded control of cell mechanics, motility, and matrix remodeling. *Biophys. J.* **102**, 434–442.
- Moore, D. S. and McCabe, G. P. (2002). *Introduction to the Practice of Statistics*. New York, NY: W. H. Freeman.
- Na, S., Collin, O., Chowdhury, F., Tay, B., Ouyang, M. X., Wang, Y. X. and Wang, N. (2008). Rapid signal transduction in living cells is a unique feature of mechanotransduction. *Proc. Natl. Acad. Sci. USA* **105**, 6626–6631.
- Plotnikov, S. V., Pasapera, A. M., Sabass, B. and Waterman, C. M. (2012). Force fluctuations within focal adhesions mediate ECM-rigidity sensing to guide directed cell migration. *Cell* **151**, 1513–1527.
- Prager-Khoutorsky, M., Lichtenstein, A., Krishnan, R., Rajendran, K., Mayo, A., Kam, Z., Geiger, B. and Bershadsky, A. D. (2011). Fibroblast polarization is a matrix-rigidity-dependent process controlled by focal adhesion mechanosensing. *Nat. Cell Biol.* **13**, 1457–1465.
- Rauzi, M., Verant, P., Lecuit, T. and Lenne, P. F. (2008). Nature and anisotropy of cortical forces orienting Drosophila tissue morphogenesis. *Nat. Cell Biol.* **10**, 1401–1410.
- Ronchi, P., Terjung, S. and Pepperkok, R. (2012). At the cutting edge: applications and perspectives of laser nanosurgery in cell biology. *Biol. Chem.* **393**, 235–248.
- Rossier, O. M., Gauthier, N., Biais, N., Vonnegut, W., Fardin, M. A., Avigan, P., Heller, E. R., Mathur, A., Ghassemi, S., Koeckert, M. S. et al. (2010). Force generated by actomyosin contraction builds bridges between adhesive contacts. *EMBO J.* **29**, 1055–1068.

- Russell, R. J., Xia, S. L., Dickinson, R. B. and Lele, T. P. (2009). Sarcomere mechanics in capillary endothelial cells. *Biophys. J.* **97**, 1578-1585.
- Sawada, Y., Tamada, M., Dubin-Thaler, B. J., Cherniavskaya, O., Sakai, R., Tanaka, S. and Sheetz, M. P. (2006). Force sensing by mechanical extension of the Src family kinase substrate p130Cas. *Cell* **127**, 1015-1026.
- Sen, S., Dong, M. and Kumar, S. (2009). Isoform-specific contributions of alpha-actinin to glioma cell mechanobiology. *PLoS ONE* **4**, e8427.
- Stricker, J., Sabass, B., Schwarz, U. S. and Gardel, M. L. (2010). Optimization of traction force microscopy for micron-sized focal adhesions. *J. Phys. Condens. Matter* **22**, 194104.
- Stricker, J., Aratyn-Schaus, Y., Oakes, P. W. and Gardel, M. L. (2011). Spatiotemporal constraints on the force-dependent growth of focal adhesions. *Biophys. J.* **100**, 2883-2893.
- Tan, J. L., Tien, J., Pirone, D. M., Gray, D. S., Bhadriraju, K. and Chen, C. S. (2003). Cells lying on a bed of microneedles: an approach to isolate mechanical force. *Proc. Natl. Acad. Sci. USA* **100**, 1484-1489.
- Tanner, K., Boudreau, A., Bissell, M. J. and Kumar, S. (2010). Dissecting regional variations in stress fiber mechanics in living cells with laser nanosurgery. *Biophys. J.* **99**, 2775-2783.
- Théry, M. (2010). Micropatterning as a tool to decipher cell morphogenesis and functions. *J. Cell Sci.* **123**, 4201-4213.
- Tinsley, R. B., Vesey, M. J., Barati, S., Rush, R. A. and Ferguson, I. A. (2004). Improved non-viral transfection of glial and adult neural stem cell lines and of primary astrocytes by combining agents with complementary modes of action. *J. Gene Med.* **6**, 1023-1032.
- Tondon, A., Hsu, H. J. and Kaunas, R. (2012). Dependence of cyclic stretch-induced stress fiber reorientation on stretch waveform. *J. Biomech.* **45**, 728-735.
- Totsukawa, G., Wu, Y., Sasaki, Y., Hartshorne, D. J., Yamakita, Y., Yamashiro, S. and Matsumura, F. (2004). Distinct roles of MLCK and ROCK in the regulation of membrane protrusions and focal adhesion dynamics during cell migration of fibroblasts. *J. Cell Biol.* **164**, 427-439.
- Vogel, V. (2006). Mechanotransduction involving multimodular proteins: converting force into biochemical signals. *Annu. Rev. Biophys. Biomol. Struct.* **35**, 459-488.
- Wang, N., Tytell, J. D. and Ingber, D. E. (2009). Mechanotransduction at a distance: mechanically coupling the extracellular matrix with the nucleus. *Nat. Rev. Mol. Cell Biol.* **10**, 75-82.
- Zamir, E., Katz, B. Z., Aota, S., Yamada, K. M., Geiger, B. and Kam, Z. (1999). Molecular diversity of cell-matrix adhesions. *J. Cell Sci.* **112**, 1655-1669.
- Zhang, C., Yadava, P. and Hughes, J. (2004). Polyethylenimine strategies for plasmid delivery to brain-derived cells. *Methods* **33**, 144-150.
- Zhong, W., Wu, M., Chang, C. W., Merrick, K. A., Merajver, S. D. and Mycek, M. A. (2007). Picosecond-resolution fluorescence lifetime imaging microscopy: a useful tool for sensing molecular interactions in vivo via FRET. *Opt. Express* **15**, 18220-18235.

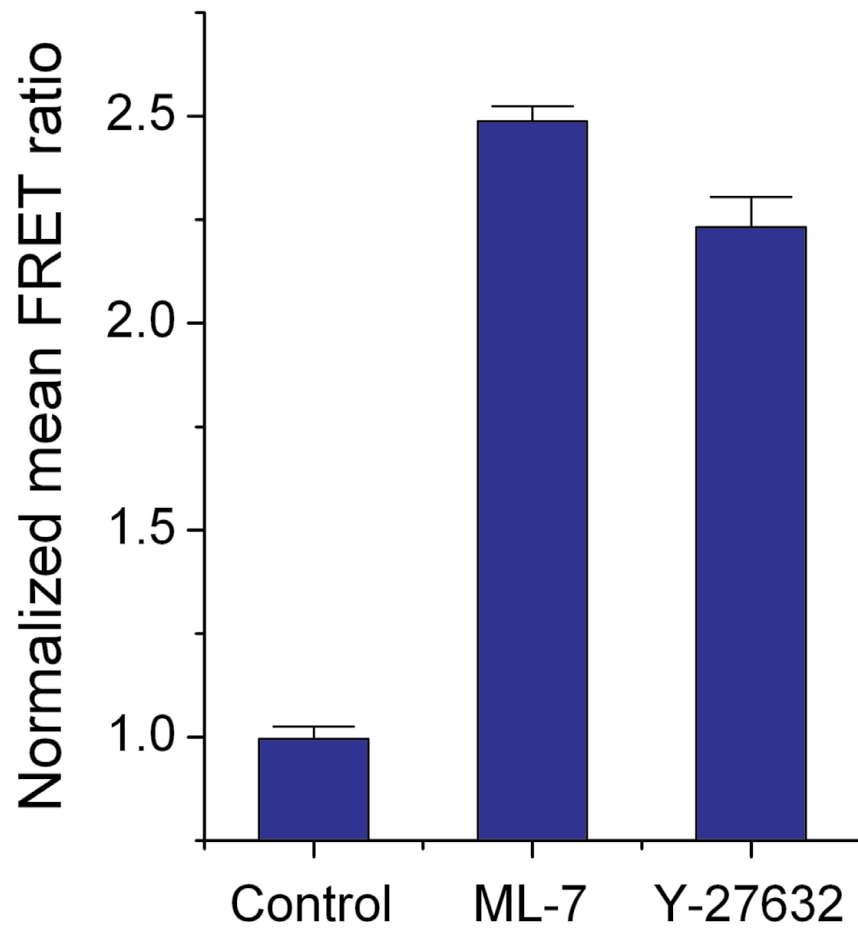


Fig. S1. VinTS FRET increases with pharmacological inhibition of tension. The bars depict overall mean VinTS FRET ratio values 60 min after drug treatment (10 μ M ML-7 or 5 μ M Y-27632) or without drug treatment (Control). The values are normalized to the corresponding FRET ratio right before the treatment at time = 0 min. N=3 cells for both ML-7 and Y-27632; N=2 cells for control.

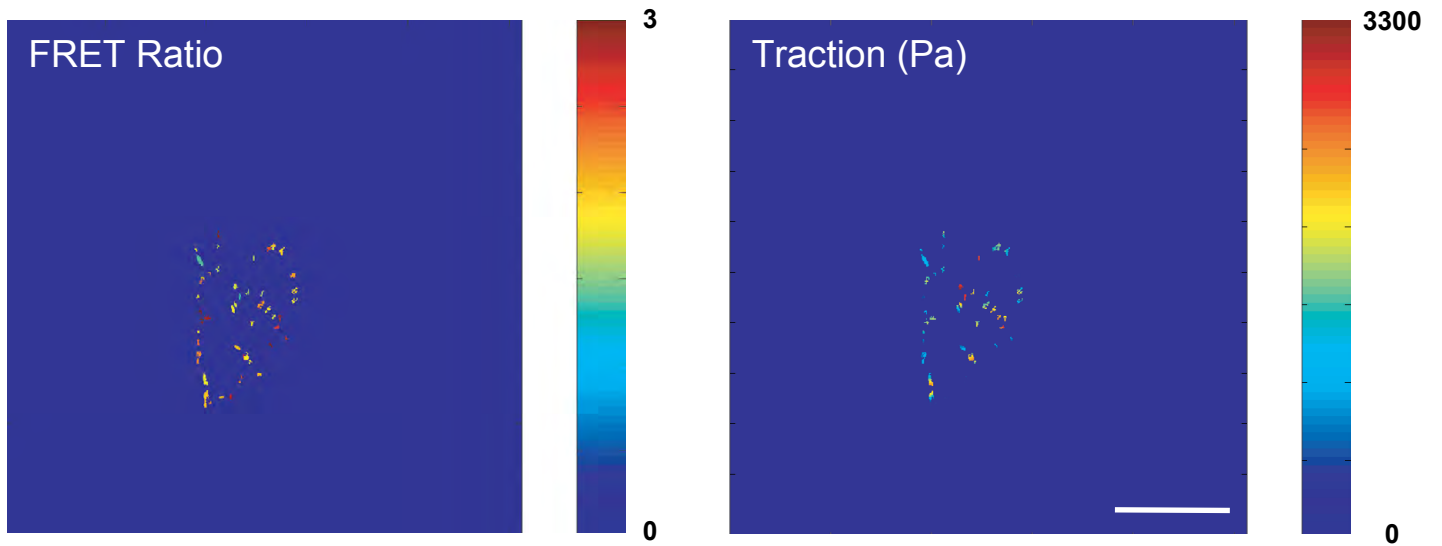
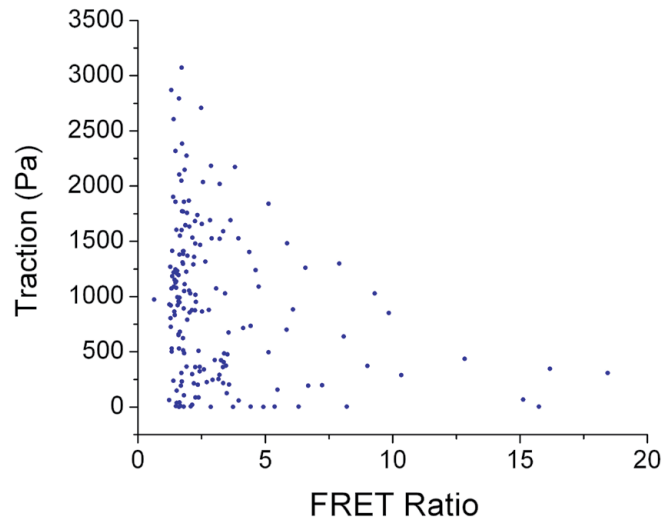


Fig. S2. Cell-ECM traction correlates with tension across FA-based vinculin. Traction force microscopy (see Materials and Methods) was performed on VinTS-expressing cells, and the resulting maps of traction force were masked using the FA-segmented VinTS image to examine potential correlations between VinTS signal and traction force at FAs (Upper) mean traction in FA-projected area versus mean FRET ratio in the corresponding FA. Each point represents a single FA, with data consisting of 175 adhesions pooled from 4 cells. The data reveal a modest inverse linear correlation between traction force and VinTS FRET ratio ($R^2=0.0733$, $P=0.00029$ against the null hypothesis of no correlation). (Lower left) FRET ratio map with FA mask for a representative cell. (Lower right) Traction force map for the same cell using the same FA mask. Scale bar: 50 μm .

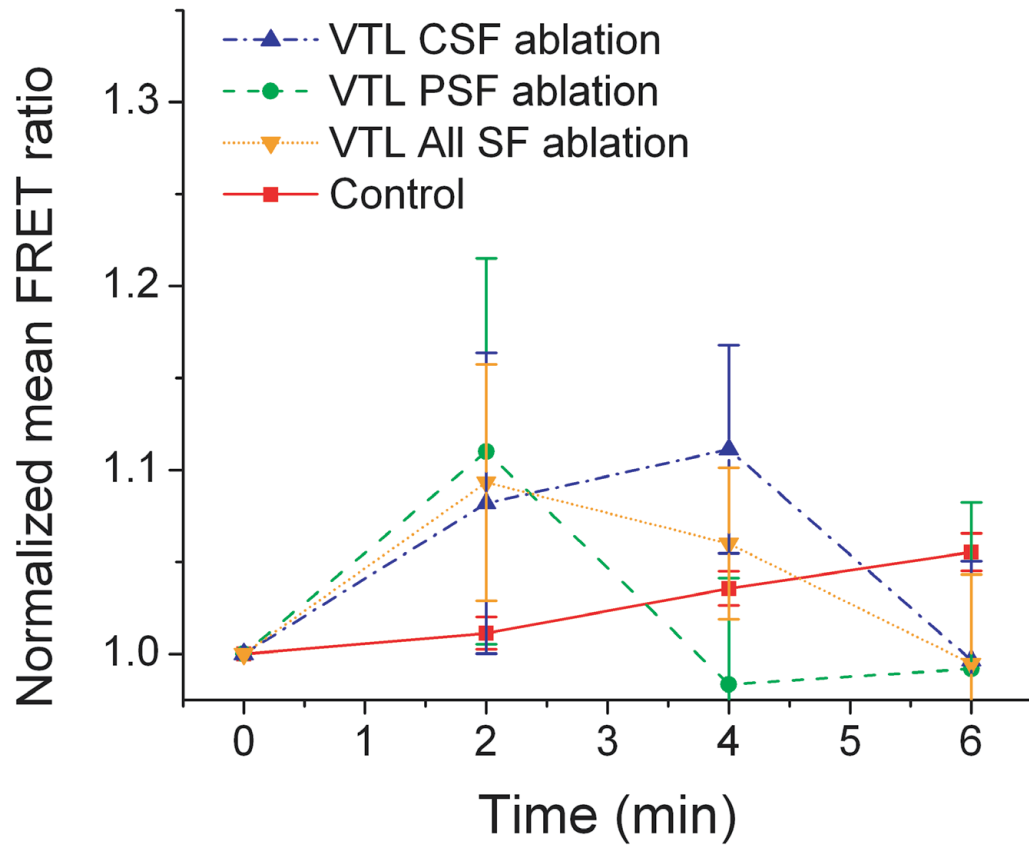


Fig. S3. Cells transfected with vinculin tail-less sensor (VTL) fail to show the ablation-dependent responses exhibited by VinTS. Overall mean FRET ratio versus time for ‘4-Image Tracking’ (see text) is shown with the values normalized to the corresponding FRET ratio at time 0 min. As expected, the FRET ratio does not change in a systematic way following SF ablation. N=8 cells for VTL peripheral SF (PSF) ablation; N=6 cells for VTL central SF (CSF) ablation.

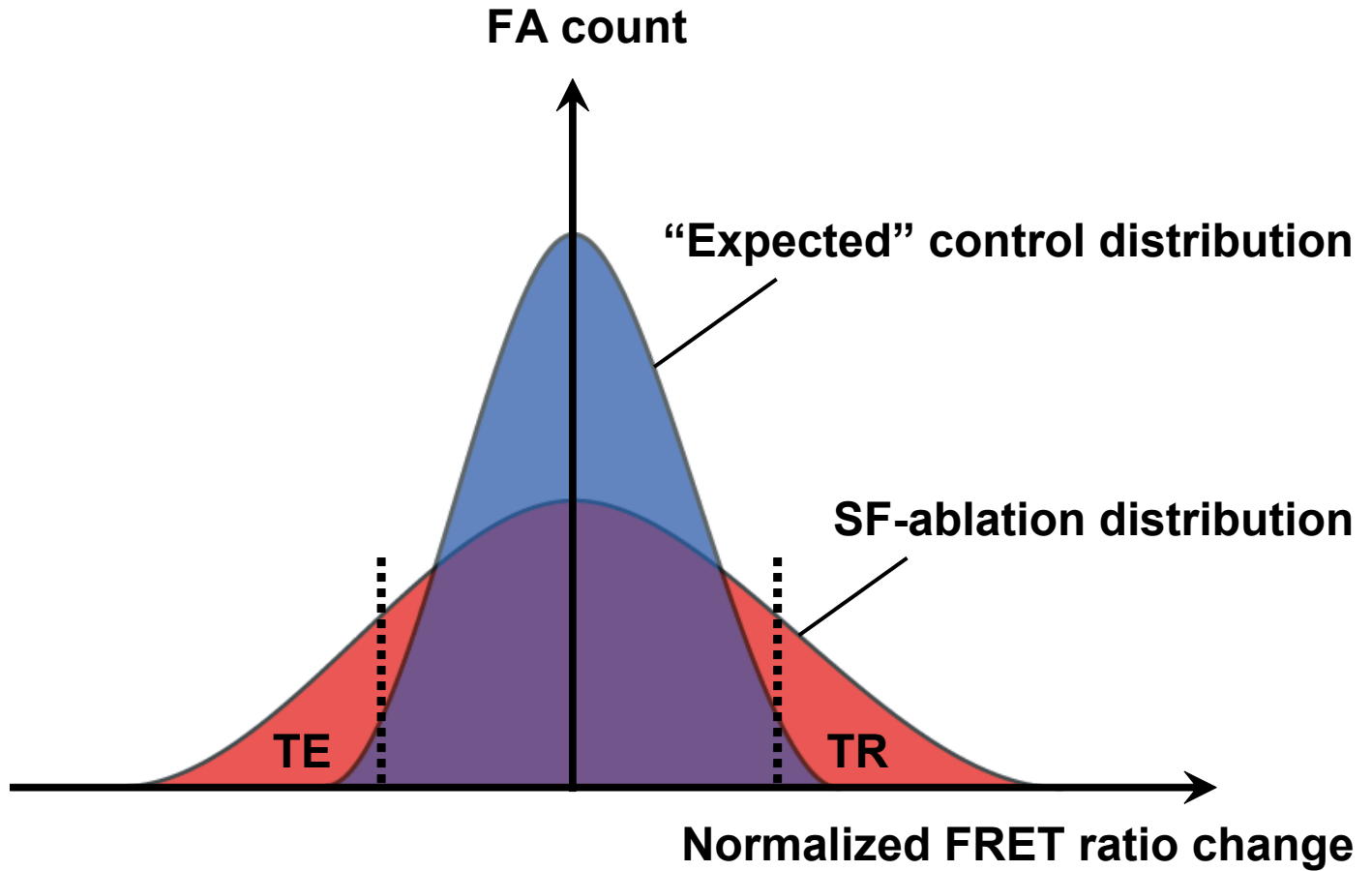


Fig. S4. Defining tension-enhanced (TE) and tension-reduced (TR) FAs. TE and TR FAs were defined based on the control (non-SF-ablated) and experimental (SF-ablated) FA distributions of normalized FRET ratio change. Since the numbers of FAs in the control groups were smaller than the experimental groups, the control distributions were first normalized to obtain distributions of equivalent size to the corresponding experimental group. In principle, all tension enhanced and tension reduced FAs should lie within the portions of the experimental distribution that do not overlap the control distribution (red areas). After testing various cutoff values to approximately capture these FAs with optimal sensitivity and specificity (supplementary material Table S1), we decided to use a 5th percentile/95th percentile threshold. In other words, FAs in the experimental group with normalized FRET ratio change values between the 5th and 95th percentiles of those of the control (the portion of the red experimental distribution between the two dashed lines) were assumed to exhibit spontaneous FRET ratio change and designated as non-TE/TR FAs. FAs whose normalized FRET ratio change exceeded the 95th percentile value for the control population were designated as tension reduced (experimental points to the right of the right dashed line). Similarly, FAs whose normalized FRET ratio change fell below the 5th percentile value of the control population were designated as tension enhanced (experimental points to the left of the left dashed line).

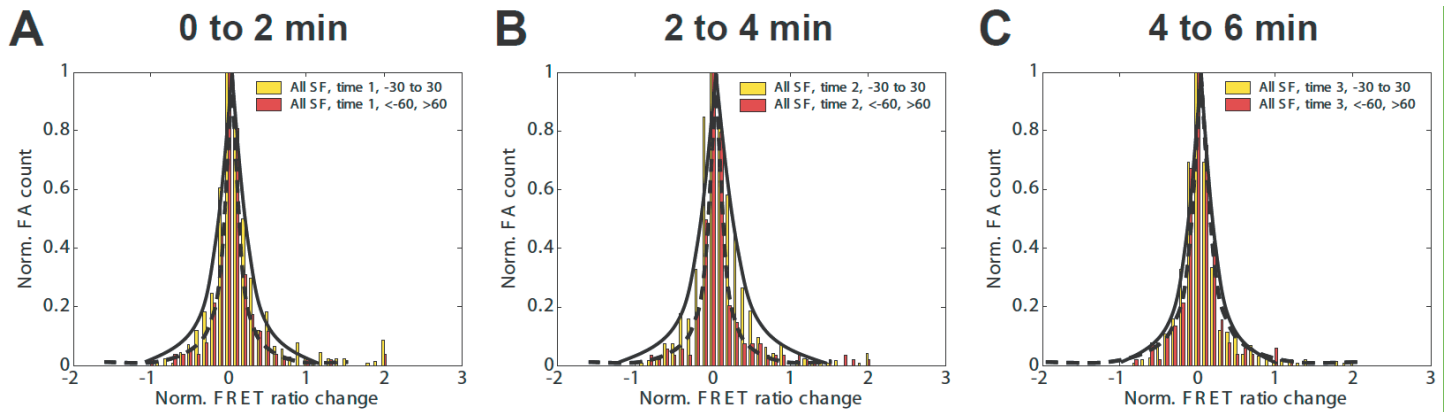


Fig. S5. Observed angle-specificity is not a sampling artifact. (A–C) Normalized FRET ratio change histograms in the specified time intervals after SF ablation. For each time interval, the two distributions ($|\text{FA angle}| < 30^\circ$ and $|\text{FA angle}| > 60^\circ$) were normalized to the maximum values to illustrate their different shapes. Note that the histograms with $|\text{FA angle}| < 30^\circ$ (yellow bars and solid curves) have wider distributions than the ones with $|\text{FA angle}| > 60^\circ$ (red bars and dashed curves), especially for the first two time intervals (A,B). This indicates that both tension enhancement and reduction have a higher chance of occurring in the $|\text{FA angle}| < 30^\circ$ group, independent of the actual numbers of FAs in those groups. This is consistent with our interpretation based on the Gaussian fit widths of the FA histograms with respect to the FA angles (Fig. 4G).

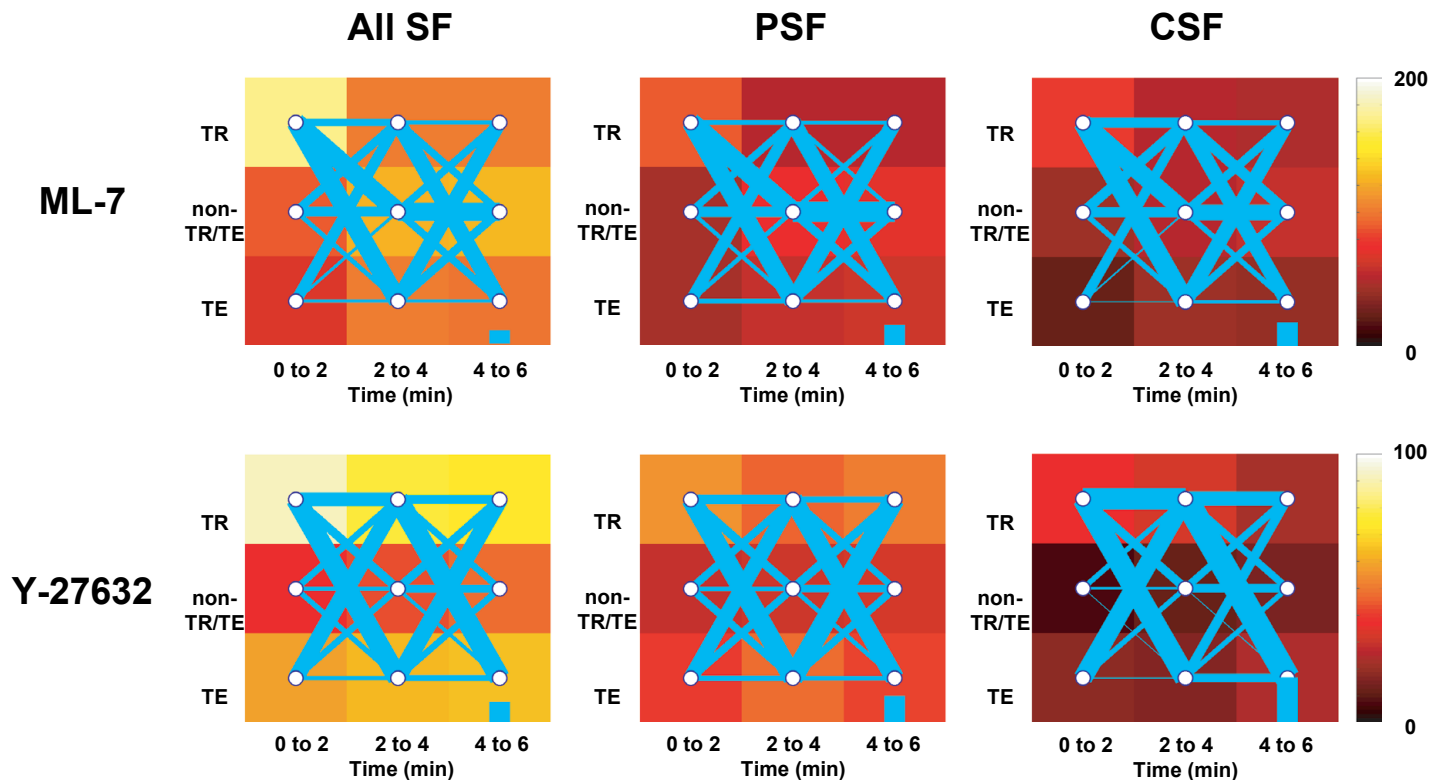
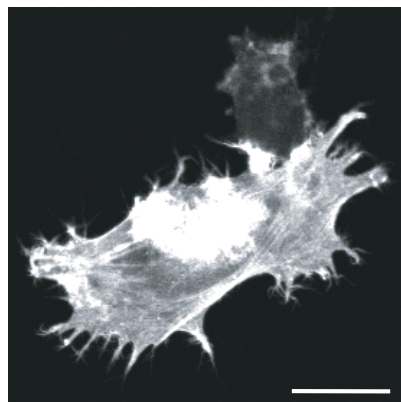
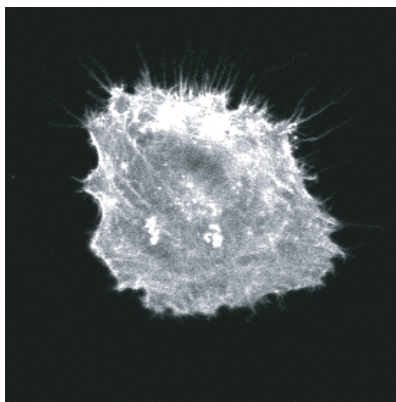
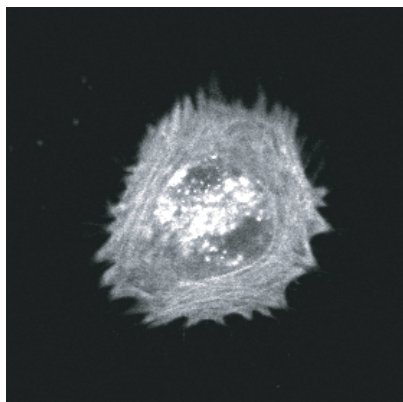


Fig. S6. Tension-reducing drugs induce more tension transitions. Tension transition diagrams (Fig. 5) are shown following pharmacologic inhibition of ROCK (5 μM Y27632) and MLCK (10 μM ML-7) for 24 hours prior to SF ablation.

**Before
Ablation**



**After
Ablation**

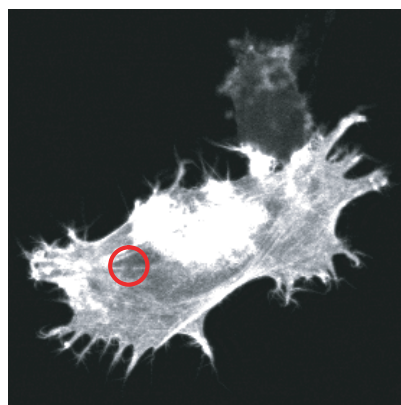
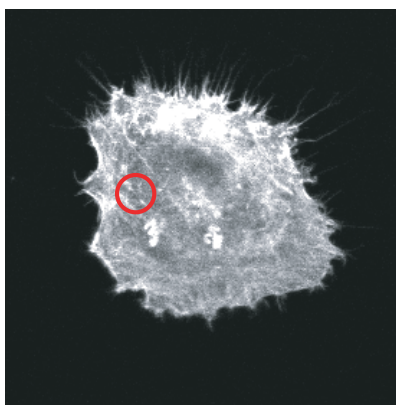
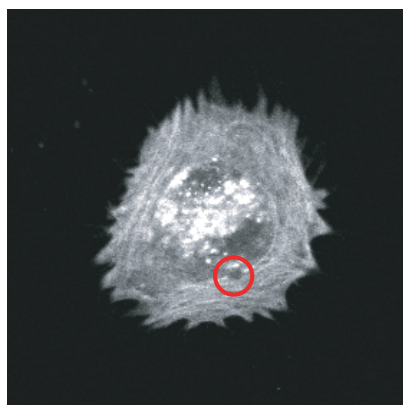


Fig. S7. Severing single SFs within an interconnected network. mCherry-Lifeact images are shown for three representative cells in which single central SFs were singly severed (incision sites marked with red circles) despite being interconnected with other SFs. Scale bar: 30 μm .

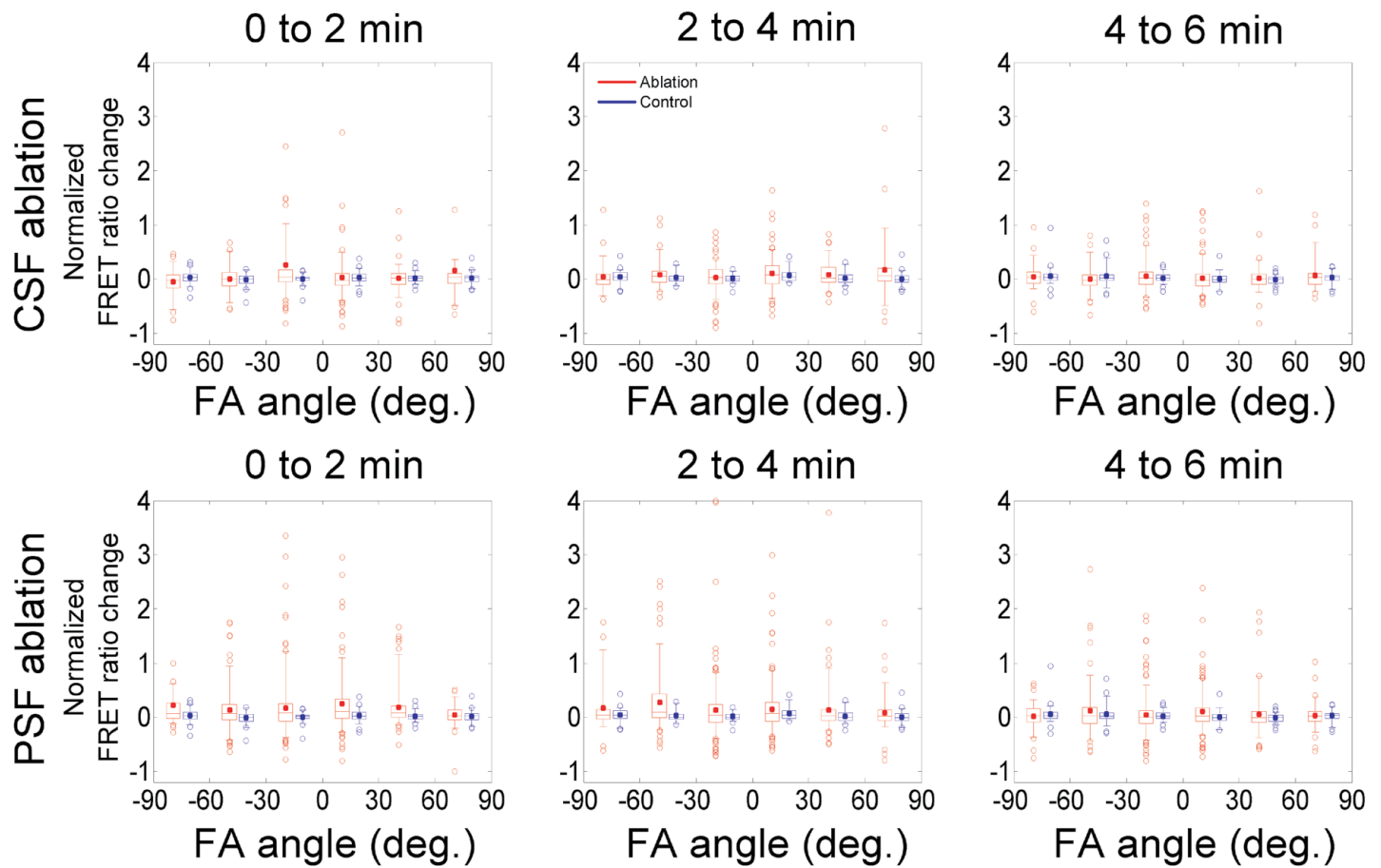


Fig. S8. Tension distribution to FAs from different subpopulations of SFs. Distributions of normalized FRET ratio changes in individual FAs following central (top row) and peripheral SF ablation (bottom row). The FRET ratio changes were calculated from 2-image FA tracking (Fig. 2C) over the indicated time intervals, and then plotted as a function of the angle between FA long axis and the reference axis (SF axis for ablated cells and cell long axis for non-ablated controls, as shown in Fig. 3A). The FRET ratio changes were normalized to the corresponding FRET ratio at the first time point of each two-minute interval. The horizontal box lines indicate 25th, 50th and 75th percentiles, the whisker ends indicate 5th and 95th percentiles, and the solid dots indicate mean values. Each data point represents one FA.

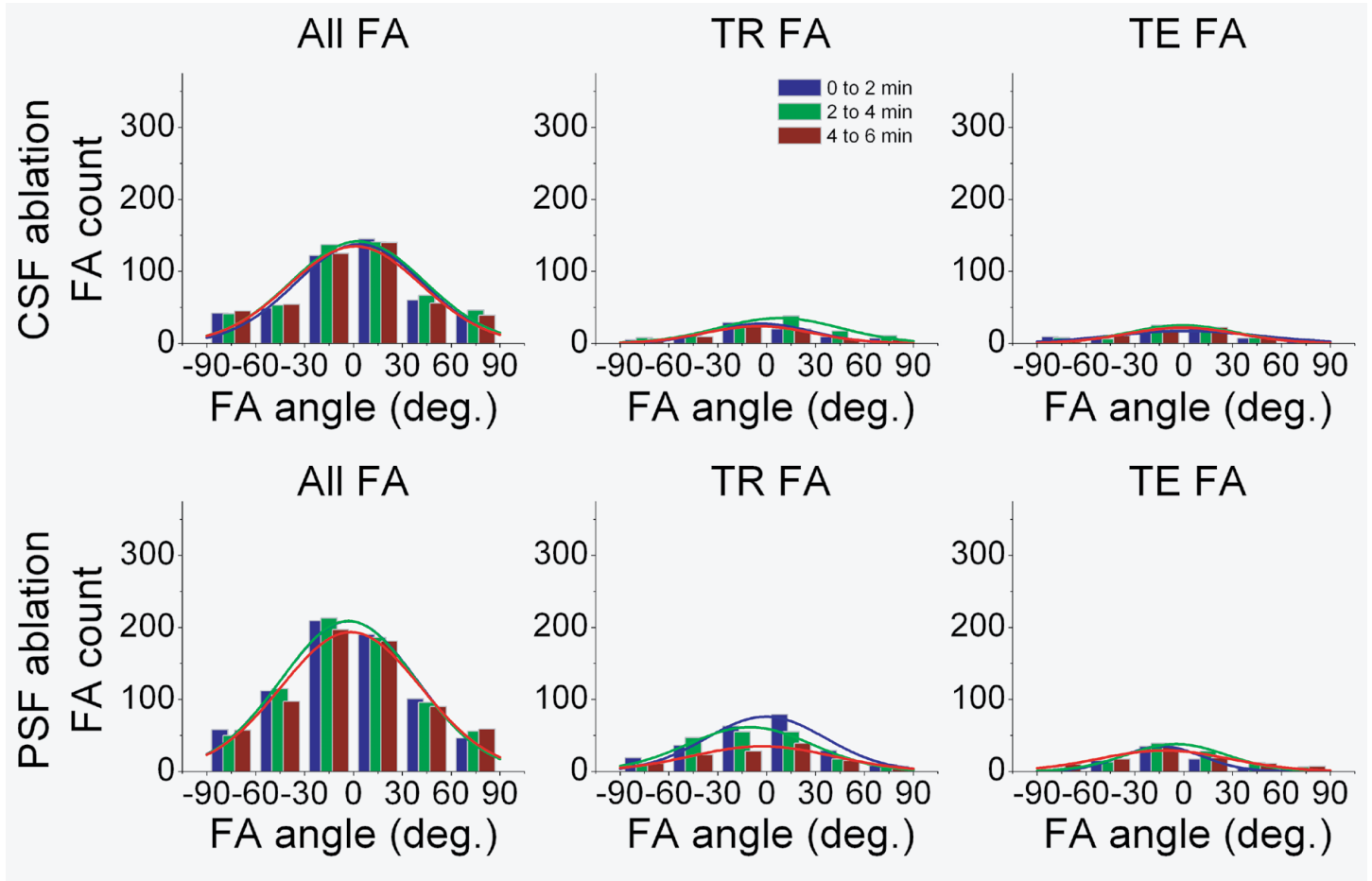


Fig. S9. Tension changes in FAs following ablation of different subpopulations of SFs. Time-dependent histograms of angles between FA and SF orientations, following photo-disruption of (top row) central and (bottom row) peripheral SF ablation. The curves are the corresponding Gaussian curve fits. The widths of the Gaussian fits are shown in Fig. 4H-I for peripheral SF and central SF ablation, respectively.

Table S1. The criteria to select TE and TR FAs and their corresponding sensitivities and specificities. The criteria (mean \pm standard deviation or percentiles) were defined based on the ‘expected’ control distribution of normalized FRET ratio change (supplementary material Fig. S1). The sensitivities and specificities are presented in percentages (%). 5th/95th percentile criteria (blue) were used for the entire study due to its 100% sensitivity for almost all cases and its high specificity.

0 to 2 min after SF photo-disruption						
<i>Criteria</i>	<i>TE threshold</i>	<i>TE sensitivity</i>	<i>TE specificity</i>	<i>TR threshold</i>	<i>TR sensitivity</i>	<i>TR specificity</i>
Mean \pm std	−0.0982	100.00	88.43	0.1270	100.00	83.80
10th/90th	−0.1188	100.00	91.13	0.1464	100.00	88.40
5th/95th	−0.1760	100.00	96.07	0.1812	97.23	93.74
1st/99th	−0.3610	52.18	99.03	0.3311	64.58	98.86
2 to 4 min after SF photo-disruption						
<i>Criteria</i>	<i>TE threshold</i>	<i>TE sensitivity</i>	<i>TE specificity</i>	<i>TR threshold</i>	<i>TR sensitivity</i>	<i>TR specificity</i>
Mean \pm std	−0.0896	100.00	85.23	0.1374	100.00	83.29
10th/90th	−0.0897	100.00	85.32	0.1632	100.00	87.20
5th/95th	−0.1375	100.00	92.65	0.2162	100.00	94.26
1st/99th	−0.2312	100.00	99.16	0.4212	56.03	98.89
4 to 6 min after SF photo-disruption						
<i>Criteria</i>	<i>TE threshold</i>	<i>TE sensitivity</i>	<i>TE specificity</i>	<i>TR threshold</i>	<i>TR sensitivity</i>	<i>TR specificity</i>
Mean \pm std	−0.1125	100.00	84.75	0.1562	100.00	87.74
10th/90th	−0.1156	100.00	85.13	0.1534	100.00	87.25
5th/95th	−0.1854	100.00	92.91	0.2091	100.00	93.57
1st/99th	−0.2692	100.00	99.07	0.5041	56.41	99.03